Temporal dynamics of the BOLD fMRI impulse response

Jacco A. de Zwart,[a],* Afonso C. Silva,[a] Peter van Gelderen,[a] Peter Kellman,[b] Masaki Fukunaga,[a] Renxin Chu,[a] Alan P. Koretsky,[a] Joseph A. Frank,[c] and Jeff H. Duyn[a]

[a]Laboratory of Functional and Molecular Imaging, NINDS, National Institutes of Health, Bethesda, MD 20892-1065, USA
[b]Laboratory of Cardiac Energetics, NHLBI, National Institutes of Health, Bethesda, MD 20892-1065, USA
[c]Laboratory of Diagnostic Radiology Research, CC, National Institutes of Health, Bethesda, MD 20892-1065, USA

Using computer simulations and high-resolution fMRI experiments in humans ($n = 6$) and rats ($n = 8$), we investigated to what extent BOLD fMRI temporal resolution is limited by dispersion in the venous vasculature. For this purpose, time-to-peak (TTP) and full-width at half-maximum (FWHM) of the BOLD impulse response (IR) function were determined. In fMRI experiments, a binary m-sequence probe method was used to obtain high-sensitivity model-free single-pixel estimates of IR. Simulations of postcapillary flow suggested that flow-related dispersion leads to a TTP and FWHM increase, which can amount to several seconds in larger pial veins. fMRI experiments showed substantial spatial variation in IR timing within human visual cortex, together with a correlation between TTP and FWHM. Averaged across the activated regions and across subjects, TTP and FWHM were 4.51 ± 0.52 and 4.04 ± 0.42 s, respectively. In regions of interest (ROI) weighted toward the larger venous structures, TTP and FWHM increased to 5.07 ± 0.64 and 4.32 ± 0.48 s, respectively. In rat somatosensory cortex, TTP and FWHM were substantially shorter than in humans (2.73 ± 0.60 and 2.28 ± 0.63 s, respectively). These results are consistent with a substantial macrovascular dispersive contribution to BOLD IR in humans, and furthermore suggest that neurovascular coupling is a relatively rapid process, with a resolution below 2.3 s FWHM.
Published by Elsevier Inc.

Keywords: BOLD fMRI; Binary m-sequence; Hemodynamic response; Vascular dispersion

Introduction

The spatial and temporal resolutions of BOLD fMRI (Ogawa et al., 1990) are limited by the underlying mechanism of contrast generation, which is based on changes in deoxyhemoglobin concentration resulting from stimulus-induced increases in cerebral blood flow that overcompensate for increases in oxygen consumption. These blood flow changes are believed to be associated with changes in synaptic activity (Logothetis et al., 2001), with chemical or electrical signals mediating arterial dilation through sphincters and capillary smooth muscle cells. Depending on the brain processes under study, changes in activity can be localized to the submillimeter columnar and laminar scales of the cerebral cortex, and can occur with temporal scales in the millisecond range. Much of this fine-scale dynamics is lost in fMRI, with its spatial resolution estimated at a few millimeters full-width at half-maximum (FWHM) (Engel et al., 1997), and the temporal resolution of the BOLD impulse response (IR) at 4–7 s FWHM (Aguirre et al., 1998; Boynton et al., 1996; Buckner, 1998; Friston et al., 1994).

Despite its relative coarse spatial and temporal resolution, BOLD fMRI can be used to detect subtle differences in spatial and temporal aspects of neuronal activity using dedicated stimulation paradigms and analysis methods. Under certain conditions, submillimeter structures such as ocular dominance columns in humans (Cheng et al., 2001) and orientation columns in cats (Duong et al., 2001) can be detected, and subsecond timing differences between activation of different functional regions can be discriminated (Menon et al., 1998; Ogawa et al., 2000).

Both sensitivity and temporal accuracy of BOLD fMRI are dependent on accurate knowledge of the temporal characteristics of its response to a change in neuronal activity. These characteristics are influenced by the timing of neurovascular control, and the oxygenation and flow characteristics of blood both in the capillary bed and the downstream venous vasculature. The relative contribution of capillary and macrovascular venous contributions is dependent on experimental circumstances such as the magnetic field strength at which the MRI experiment is performed and of its acquisition parameters.

Previous studies have shown that the temporal characteristics of BOLD fMRI vary across subjects (Aguirre et al., 1998; Kim et al., 1997; Lee et al., 1995; Miezin et al., 2000) and functional regions (Kruggel and von Cramon, 1999; Miezin et al., 2000; Thierry et al.,

* Corresponding author. Advanced MRI section, LFMI, NINDS, National Institutes of Health, Building 10, Room B1D-728, 9000 Rockville Pike, Bethesda, MD 20892-1065, USA. Fax: +1 301 480 1981.
 E-mail address: Jacco.deZwart@nih.gov (J.A. de Zwart).
 Available online on ScienceDirect (www.sciencedirect.com).

1999). Even within a functional region, significant spread in delay between stimulus and response has been observed (Lee et al., 1995; Pfeuffer et al., 2002). Using a BOLD fMRI technique that is rather sensitive to macrovascular contributions, Lee et al. (1995) suggested that the finite transit time of blood through the macrovasculature can lead to a substantial amount of the spread in response delay within a functional region.

The potential presence of a hemodynamics-dominated response delay in fMRI has important implications for experimental design and analysis, as well as the accuracy and interpretation of fMRI-derived estimates of the timing of neuronal processes. Furthermore, it raises the question whether other aspects of the impulse response (IR), such as its width, might also be affected by hemodynamics, and how much of the response delay and broadening is related to hemodynamics in the macrovasculature rather than the sluggishness of neurovascular control. Note that BOLD signals associated with large veins partly originate from extravascular spins experiencing the fringe field of this large vessel (Duong et al., 2003). Response broadening due to hemodynamics should be reduced in areas without large (pial) vessels. In the following, we have tried to address these questions by performing computer simulations of the hemoglobin transit through the cerebral vasculature and by measuring the BOLD IR using an *m*-sequence probe (Kellman et al., 2003) in fMRI experiments at high spatial resolution in the human visual and rat somatosensory cortex.

Background

BOLD signal generation model

To analyze BOLD temporal dynamics, the following chain of sequential processes that generates the BOLD fMRI response is envisioned: a neuronal process resulting in increased synaptic activity, followed by a neurovascular mechanism increasing blood flow through control of arterial and capillary diameter, leading to an increase in oxyhemoglobin in the capillary bed, and thus to an increase in oxyhemoglobin concentration in the postcapillary (venous) vasculature. The oxyhemoglobin concentration is dependent on the imbalance between changes in blood flow (Hoge et al., 1999) and blood volume (Belliveau et al., 1991) on one side and increases or decreases in oxygen consumption on the other. The net effect of these changes, a decrease in deoxyhemoglobin in both capillary bed and venous vasculature, results in a BOLD fMRI signal increase during activation. The combined effect of these processes is generally referred to as hemodynamic response (HDR). This terminology is strictly speaking imprecise since it ignores the potential importance of the neurovascular coupling process. The IR as measured in this work includes effects of both the HDR and neurovascular coupling mechanisms.

The neuronal processes, including synaptic activity, induced by a sensory input impulse, are relatively rapid. In sensory systems, their time-scale does not exceed a few hundred milliseconds, which is substantially shorter than the seconds-long BOLD impulse response. In the following, we assume an infinitely short synaptic IR.

Following an increase in synaptic activity, capillary or arteriolar diameter is increased by pericytes and smooth muscle cells on the endothelium (Nakai et al., 1981; Nehls and Drenckhahn, 1993). Although the mechanism for this has not been firmly established, it possibly includes a combination of chemical signaling through astrocytes (Zonta et al., 2003), and signaling through direct connections between neurons and pericytes (Krimer et al., 1998; Reinhard et al., 1979; Segal and Duling, 1986; Vaucher and Hamel, 1995). The time scale of these processes is not well known and is hard to determine experimentally. Fluorescence measurements of hemoglobin flow changes in single capillaries in mid- to superficial
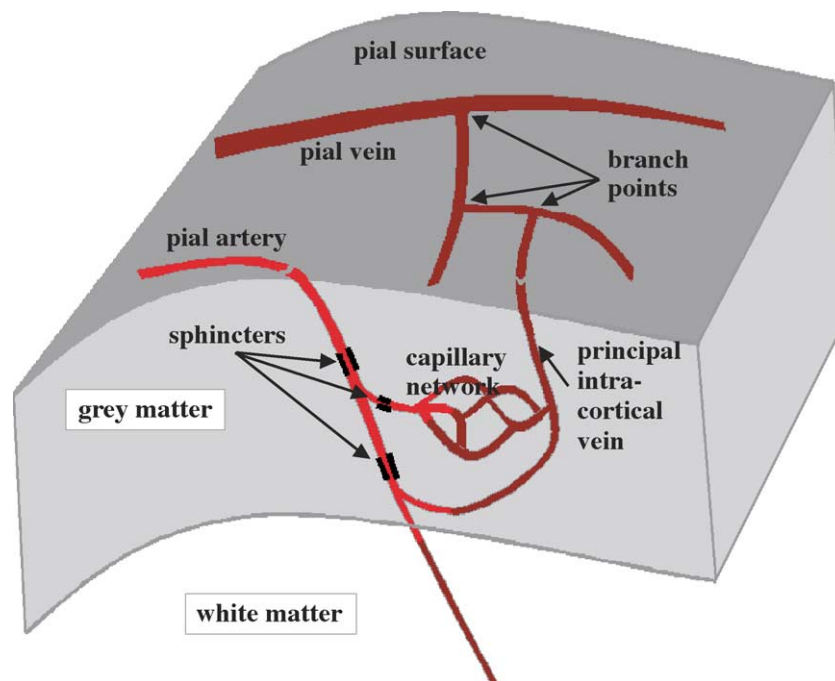

Fig. 1. Model of the dispersion along the venous flow path. Flow increases, resulting from opening of sphincters, generate an oxyhemoglobin concentration change that is carried down the vascular network. The temporal characteristics of the MRI signal, related to the local oxyhemoglobin concentration, are affected by flow characteristics along the venous flow path, with incremental signal delays accumulated in capillary bed, intracortical veins, and pial vasculature.

layers in rat cortex suggest a response width of 2–3 s FWHM. Optical imaging spectroscopy measurements of capillary dilation induced flow changes in cats and macaque (Shoham and Grinvald, 2001) and rats (Berwick et al., 2002), and laser speckle measurements in rats (Dunn et al., 2003) show a similar time-scale. However, these measurements are likely to overestimate the time-scale of neurovascular control (vascular dilation) due to effects of anesthesia (Cohen et al., 2002) or dispersion across and along the capillary bed.

The time scale of oxyhemoglobin increase in the capillaries following vascular dilation is dependent on the structure of the capillary bed as well as the flow velocity and flow path of the oxyhemoglobin molecules. Estimates of average hemoglobin flow velocities in rat capillaries vary from 0.5 to 1.5 mm s^{-1} (Hudetz et al., 1995; Kleinfeld et al., 1998; Villringer et al., 1994), and measurements in mice show a capillary transit time of 0.7 s FWHM (Rosenblum, 1971). Measurements based on arterial contrast bolus injections suggest a plasma transit time of around 1 s in rats (Rudin et al., 1997).

Additional temporal dispersion potentially occurs in the macrovasculature. After exiting the capillary bed, hemoglobin molecules travel through intracortical veins to the larger (pial) veins that transfer blood over the cortical surface (Fig. 1). The pial veins form a tree-like structure (Duvernoy et al., 1981; Turner, 2002), with slow flow in smaller and thinner veins, branching into larger, wider veins with increased flow velocity (Ma et al., 1974). This process potentially adds several seconds of delay to the observed IR and can result in a spatial variation in IR characteristics, as will be shown in the following.

Methods

Computer simulations of macrovascular transit

To estimate the temporal dispersion due to the transit of deoxyhemoglobin through the vasculature downstream from the capillary bed, Monte Carlo simulations were performed using IDL (RSI Inc., Boulder, CO, USA). In analogy with the representation of Turner (2002), the venous vasculature was modeled as a tree, originating at the exit of the capillary bed, with the finest branches (intracortical veins) combining into the principal intracortical veins (PIV) and the larger branches representing the venules and veins further downstream. It was assumed that laminar flow occurs along each vascular segment and that local turbulence causes 100% mixing of laminae at the merging point of two venules (indicated by "mix points" in the following). The equations on which the simulations are based are described in Appendix A.

The simulation was performed by averaging the behavior of 4,194,304 (4 × 1024 × 1024) 'particles'. Overall latency for each particle was derived by integrating their arrival time at 8192 discrete steps along the venous pathway. The mix points are a subset of this, particles at each of those locations are allocated a new position within the vein. This random reallocation accounts for the distribution of particles as a function of radius. To avoid particles getting stuck against the vessel wall, the minimum velocity at the vessel wall was set to 50 μm s^{-1}. At the given path lengths, the passage of the bolus is monitored by computing the number of particles that reaches this point in windows (bins) of 10 ms.

Note that this simplistic model simulates postcapillary spread of a bolus through a rigid vascular bed. It is used to model one of the factors contributing to observed spatial BOLD IR variation (postcapillary 'plumbing differences') and ignores other contributions like blood volume changes (which would 'compress' or 'stretch' the curves found with these simulations) and everything occurring in the arterial and capillary domain.

BOLD fMRI at high spatial resolution in human visual cortex

To measure temporal dispersion of the BOLD signal in the macrovasculature, human MRI studies were performed on a 3.0-T MRI system (General Electric, Milwaukee, WI, USA) equipped with CRM whole body gradients capable of generating a strength of 40 mT m^{-1} and a slew-rate of 150 T m^{-1} s^{-1}. To allow high-resolution fMRI, image signal-to-noise ratio (SNR) was boosted by employing multichannel MRI with a custom-built helmet-type 16-channel receive array that fits tightly around the head (de Zwart et al., 2004), connected to a custom-built 16-channel MRI receiver (Bodurka et al., 2004). To optimize temporal resolution and signal stability, single-shot rate-2 sensitivity-encoded (SENSE) (Pruessmann et al., 1999) echo-planar imaging (EPI) (de Zwart et al., 2002) was employed for fMRI acquisition. The combination of the dedicated receive array with SENSE EPI allowed a 2- to 4-fold improved SNR and a 50% reduction in geometric distortions relative to a conventional setup with birdcage head coil (de Zwart et al., 2004). The EPI matrix size was 192 × 144 and the field-of-view (FOV) 220 × 165 mm^2, therefore leading to a nominal in-plane resolution of 1.15 × 1.15 mm^2. A 50% ramp-sampling fraction was used to limit the readout duration (image acquisition time) to 72.3 ms. Slice thickness was 3.5 mm, slice gap was 0.5 mm. Echo time (TE) was 45 ms, repetition time (TR) 1000 ms, and flip angle 70°. A bipolar crusher gradient (with a b-value of 0.23 s mm^{-2}), placed before the EPI read-out window, was applied in the slice-select direction to reduce the contribution from large vessels (inflow effects). Using these scan parameters, image SNR (under steady state conditions) varied between 40 and 90 in cortical areas. Seven to ten 3.5-mm-thick oblique slices were selected parallel to the calcarine sulcus to include the early visual areas V1 and V2 (Brodmann areas 17 and 18).

In order to measure the BOLD fMRI IR with high sensitivity, a binary m-sequence was used to control the stimulus presentation (Kellman et al., 2003; see Fig. 2). The binary m-sequence allows efficient estimation of IR characteristics (Buracas and Boynton, 2002; Sutter, 2001). A 255-bin m-sequence with favorable properties for IR estimation was selected (Kellman et al., 2003), and a base period (bin duration) of 1000 ms was used. The 0 values of this pseudorandom sequence corresponded to the presentation of a uniform grey disk, shown for 1000 ms, whereas the 1 values corresponded to 800-ms presentation of a black and white checkerboard, contrast reversing at 7.5 Hz, followed by 200 ms of uniform grey disc. This particular design was chosen to elicit a robust neuronal response, without generating substantial neuronal nonlinearities (Kellman et al., 2003). The total experiment length was 600 s, which included an inverse repeat of the m-sequence and additional repetitions to estimate the B$_1$ sensitivity maps for SENSE reconstruction (de Zwart et al., 2002).

The check size of the checkerboard stimulus increased with eccentricity (logarithmic size increase as a function of the ring number) to elicit a strong response at all eccentricities. The luminance of the grey disc was equated to the average luminance of the checkerboard by generating them from a black and white checkerboard with number of checks equal to the projector's
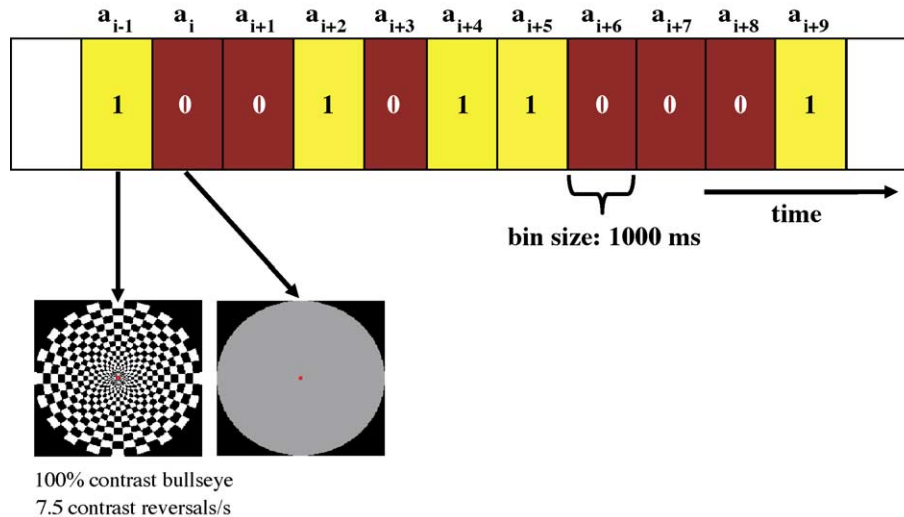
Fig. 2. The fMRI stimulus paradigm. The fMRI stimuli were controlled by a pseudo-random binary sequence (*m*-sequence). Sequential *m* sequence bins a_1 through a_{255} corresponded to active ($a_i = 1$) or rest ($a_i = 0$) stimuli. For human fMRI, the base period (bin size) was 1000 ms. The active stimulus consisted of 800 ms of checkerboard reversals (133 ms per cycle) followed by 200 ms of uniform grey disc, and a rest stimulus was 1000 ms of uniform grey disc. For rat fMRI, 500 or 1000 ms base periods were used. The active stimuli were two (for 500 ms base period) or three (for 1000 ms base period) electrical pulses of 333 μs duration, spaced respectively, 250 or 333 ms. Electrical pulses were administered to the left forepaw. During rest bins no electrical pulses were applied.

resolution (800 × 600). Flicker photometry was used to confirm the effectiveness of this approach. To encourage fixation, the color of the fixation point changed between red and pink over the course of an experiment, and the subject was asked to (silently) count the number of color changes and report this number afterwards. The visual stimuli were back-projected onto a translucent screen using an InFocus LP340 DLP projector (InFocus, Wilsonville, OR, USA). The maximum eccentricity was 10° (half diameter) and the maximum luminance (white checks) was 440 Cd m^{-2}, as measured with a Minolta LS-100 luminance meter (Konica Minolta Holdings, Inc., Tokyo, Japan). The stimulus display was generated using Presentation software (Neurobehavioral Systems, Inc., Albany, CA, USA), running on an AMD Athlon XP 2000+ based PC (Windows XP Pro), and synchronized to the MRI scanner at the end of each TR interval. Timing errors between stimulus presentation and data acquisition were small and did not exceed 20 ms over the course of the experiment (600 s).

Prior to each scan session, normal volunteers (four males, two females, aged 22.5–56.0 years, 34.8 years average) gave written, informed consent to participate in the study, which was approved by the Intramural Review Board (IRB) at the National Institutes of Health under protocol number 00-N-0082. Two of the volunteers were scanned twice, one volunteer three times, leading to a total of 11 data sets. Because of the excessive acoustic noise generated by the MRI gradient system, earplugs were provided for hearing protection.

fMRI at high spatial resolution in rat sensory cortex

To measure BOLD temporal dynamics at further reduced voxel sizes, fMRI of forepaw stimulation in rat was performed using a 31-cm diameter, horizontal bore, 11.7-T magnet (Magnex Scientific, Ltd., Abingdon, UK) interfaced to a Biospec-Avance console (Bruker, Billerica, MA) and equipped with a 9-cm gradient set capable of providing 450 mT m^{-1} within 75 μs rise time. A 7-cm diameter shielded birdcage RF coil was used for excitation, while signal reception was performed with an actively decoupled 15-mm

diameter surface coil. The increased SNR available due to the higher magnetic field strength and the smaller reception coil, in combination with the small FOV and increased performance of the smaller gradient system, facilitated fMRI at submillimeter resolution. Cortical thickness is not dramatically reduced in rat somatosensory cortex (1.8–2.2 mm) compared to human visual cortex (2–3 mm), making it possible to extract grey matter signals without substantial contamination from the pial vasculature.

All procedures performed on the animals were in strict accordance with the National Institutes of Health 'Guide for Care and Use of Laboratory Animals' and approved by the local Animal Care and Use Committee. Adult male Sprague–Dawley rats (196 ± 34 g, $n = 8$) were initially anesthetized with isoflurane and orally intubated. Arterial and venous femoral catheters were inserted for sampling of blood gases and injection of drugs. The animals were placed on an in-house built, stereotaxic, MR-compatible head holder comprising ear pieces and a bite bar to prevent head movement. For somatosensory stimulation, two needle electrodes were inserted under the skin of the left forepaw (one in the space between digits 2 and 3, the other between digits 4 and 5). Continuous physiological monitoring was employed, including measurement of expired end-tidal CO_2, rectal temperature, and blood pressure. Blood gases were measured at regular intervals and maintained at normal levels. In the magnet, anesthesia was maintained by using a continuous α-chloralose infusion (Silva and Koretsky, 2002).

Functional MRI experiments were performed using a gradient-echo EPI sequence with the following parameters: 25.6 × 12.8 mm^2 FOV; 96 × 48 matrix; 1 mm slice thickness; 267 × 267 × 1000 μm^3 nominal spatial resolution; 333 kHz acquisition bandwidth; 16.0 or 20.0 ms TE; 500 or 1000 ms TR; 13.8 ms acquisition window length. Signal was sampled on the ramps (80-μs duration each) and subsequently interpolated. To allow estimation of the fMRI impulse response (IR) FWHM, bilateral electrical stimulation of the forelimb was performed using a *m*-sequence stimulus, synchronized with the scanner, and controlled from a PC running Presentation software on Windows 2000. As in

the human fMRI experiments, a 255-bin binary m-sequence was used. The base period used was either 500 or 1000 ms. Each m-sequence 1 corresponded to a train of two or three electrical stimuli of 333-μs length with 250- or 333-ms separation, respectively. No stimulus was delivered during m-sequence 0s. The m-sequence was repeated twice (inverse repeat), and the total time for each run (including additional start and tail periods) was 300 or 600 s for the stimulus with 500 and 1000 ms base period, respectively. Two runs were performed on each rat, resulting in a total scan time of 10 and 20 min, respectively.

The electrical stimuli were delivered using a multichannel stimulator (World Precision Instruments, Sarasota, FL, USA). Their amplitude was set to 2 mA, which was safely below the threshold for induced twitching of the animal (Silva et al., 1999). Stimuli were synchronized from the scanner at the end of each TR interval and delivered to the animal through the parallel port of the PC running the Presentation software. Timing errors between electrical pulse delivery to the animal and image acquisition were small (below 19 ms).

Data analysis

All human 3-T MRI data were analyzed off-line on a multi-node Linux/PC reconstruction cluster (1 master and 12 slave computers, each with dual Intel Xeon processors) using IDL. For the human experiments, image reconstruction was performed as described previously and included direct Fourier transform of the ramp-sampled data, EPI ghost correction using a navigator echo (Bruder et al., 1992), and SENSE unfolding as well as image intensity correction based on coil sensitivity reference maps derived from the array data itself (de Zwart et al., 2002). Image reconstruction for the animal experiments was performed on the Bruker spectrometer console.

Analysis of brain activation was performed by cross-correlating the m-sequence input paradigm with the time-course of the image intensity on a pixel-by-pixel basis, for all possible temporal lags (Kellman et al., 2003). This was done by multiplication in Fourier domain after high-pass filtering with a cut-off at 0.008 Hz. Subsequently, significantly activated voxels were selected from t statistics. This involved integrating the IR (first order kernel) over a lag range of 1–4 s (for rat data) or 2–6 s (for human data). These regions were determined pragmatically from inspection of the correlation data. t values were generated by dividing the IR integrals by an estimate of the temporal noise level (temporal standard deviation) obtained from an area in the correlogram without any (first or higher order) correlation peaks. All pixels with t values exceeding 4.0 were considered significantly activated and used for further analysis. Although the m-sequence probe method allows measurement of linear and nonlinear Wiener kernel coefficients (Kellman et al., 2003), in this work only the linear kernel was analyzed.

For each of the activated pixels, time-to-peak (TTP) and FWHM of the IR were calculated after 12-fold Fourier interpolation of the correlograms. This was done by determining the time point with maximum value and subsequently assigning the time points (and their difference) with half maximum values. This procedure avoided having to resort to model fit procedures, which carry the risk of introducing a systematic error (bias). The TTP values were calculated starting from the beginning of the stimulus bin. To investigate shape differences between early and late peaking IRs, selective averaging was

performed by sorting the responses on TTP value and averaging over 1-s TTP bins.

To determine whether TTP and FWHM of the BOLD IR were different between activation in large venous structures and in other brain areas, a region of interest (ROI) weighted toward large veins was determined. This was done by dividing the baseline image intensity (at $t = 10$ s) by the temporal noise level (see above). In the resulting map, veins show up bright, since their image intensity is low (under the experimental conditions described above) and their temporal noise level high. A vein-weighted ROI was generated by thresholding on each subject, the threshold level was adjusted as to select a subgroup of 15% of the pixels in the activated region.

Results

Simulations of macrovascular transit

The computer simulations of the transit of the stimulus-induced deoxyhemoglobin change through the venous vasculature showed a dispersive character, with both TTP and FWHM of the IR increasing with postcapillary path length. TTP and FWHM values were inversely proportional to the capillary red blood cell (RBC) flow velocity. Fig. 3 shows an example for an average RBC flow velocity of 0.5 mm s^{-1} at the exit of the capillary bed (5-μm diameter vessels). The input parameters are in the range of values found in anesthetized rats (Chaigneau et al., 2003; Kleinfeld et al., 1998; Krolo and Hudetz, 2000; Ma et al., 1974). No in vivo data on capillary flow velocities in humans were found in the literature. Note that RBC flow velocity in human cortical vasculature might be different between human and rat, as it depends on several factors (e.g., the local pressure gradient and capillary geometry). Starting from an impulse change of deoxyhemoglobin at the input of the venous tree at the exit of the capillary bed, the impulse broadens into a gamma-variate-like function.

Based on these parameters, the value for k in Eq. (A4) in Appendix A is 16.1. The locations of the mixing points were
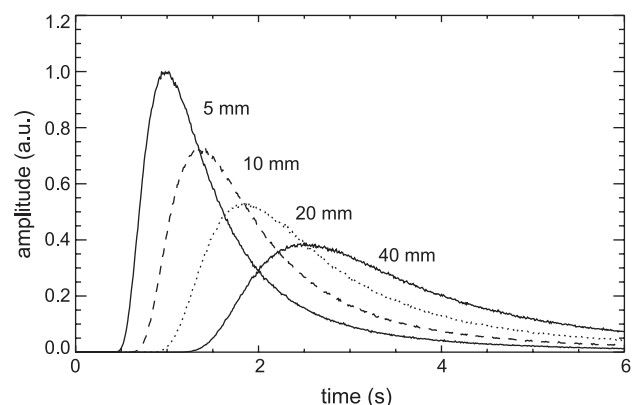

Fig. 3. Results of a Monte Carlo simulation of IR delays that are incurred in the postcapillary vasculature. With increasing downstream distance from the exit of the capillary bed, an impulse-labeled bolus (e.g., an oxy-hemoglobin concentration increase) experiences progressively increasing dispersion (delay concurrent with broadening). Depending on flow velocity at the emergence point (in this example 0.5 mm s^{-1} average flow velocity for 5-μm diameter capillaries was assumed), IR delay and width can exceed 1 s for path lengths of less than 10 mm. Delay and dispersion are shown for path lengths of 5, 10, 20, and 40 mm.

Table 1
Temporal characteristics of BOLD fMRI IR in humans

Run no. (subject no.; age; sex)	TTP (s)	TTP SD (s)	FWHM (s)	FWHM SD (s)	TTP vs. BOLD correlation	TTP BOLD vs. FWHM BOLD fit		No. of pixels
						slope	slope SD	
1 (1; 31; M)	4.78	0.85	4.18	0.84	0.45	0.76	0.03	2000
2 (2; 30; M)	4.42	0.81	4.38	1.00	0.28	2.02	0.12	1734
3 (3; 56; F)	3.99	0.60	3.66	0.81	0.13	4.87	1.08	811
4 (4; 22; F)	5.72	1.05	4.89	1.20	0.25	1.63	0.14	964
5 (5; 37; M)	5.02	0.93	4.41	0.98	0.25	1.26	0.11	960
6 (3)	4.23	0.74	3.69	0.81	0.27	0.84	0.10	675
7 (2)	4.50	0.70	3.62	0.68	0.15	0.80	0.08	1189
8 (4)	4.57	0.86	4.18	0.78	0.33	0.77	0.06	641
9 (3)	4.37	0.70	3.44	0.59	0.30	0.58	0.03	2270
10 (6; 33; M)	4.00	0.71	3.92	0.59	0.20	0.44	0.04	1218
11 (6)	4.02	0.75	4.01	0.58	0.22	0.36	0.04	969
Average (SD)	4.51 (0.52)	0.79	4.04 (0.42)	0.79	0.26 (0.09)	1.32 (1.28)		1221 (545)

derived based on Eq. (A6) (Appendix A), starting from the capillary diameter (5 μm). For the capillary flow parameters used here, 20 mix points were found to cover the simulated flow path length of 40 mm. (The path lengths of 5, 10, and 20 mm encompassed, respectively, 14, 16, and 18 mix points and represent, respectively, the first one-eighth, quarter, and half of the 40-mm flow path.) Computed mix point locations were rounded off to the nearest (8192) discrete steps along the vein. The resulting length of the first (shortest) simulated segment (the distance from the capillary bed to the first mix point) was 15 μm.

For distances between 5 and 40 mm, FWHM ranges from 0.9 to 2.3 s and TTP from 0.9 to 2.5 s. Note that TTP and especially FWHM are somewhat sensitive to the number and the location of simulated mixing points. In one extreme, a very large number of mixing points will lead to an approximately Gaussian distribution around the average arrival time. In the other extreme, absence of mixing points, the average arrival time will be identical but TTP will be reduced and the spread of arrival times, and thus FWHM, will increase.
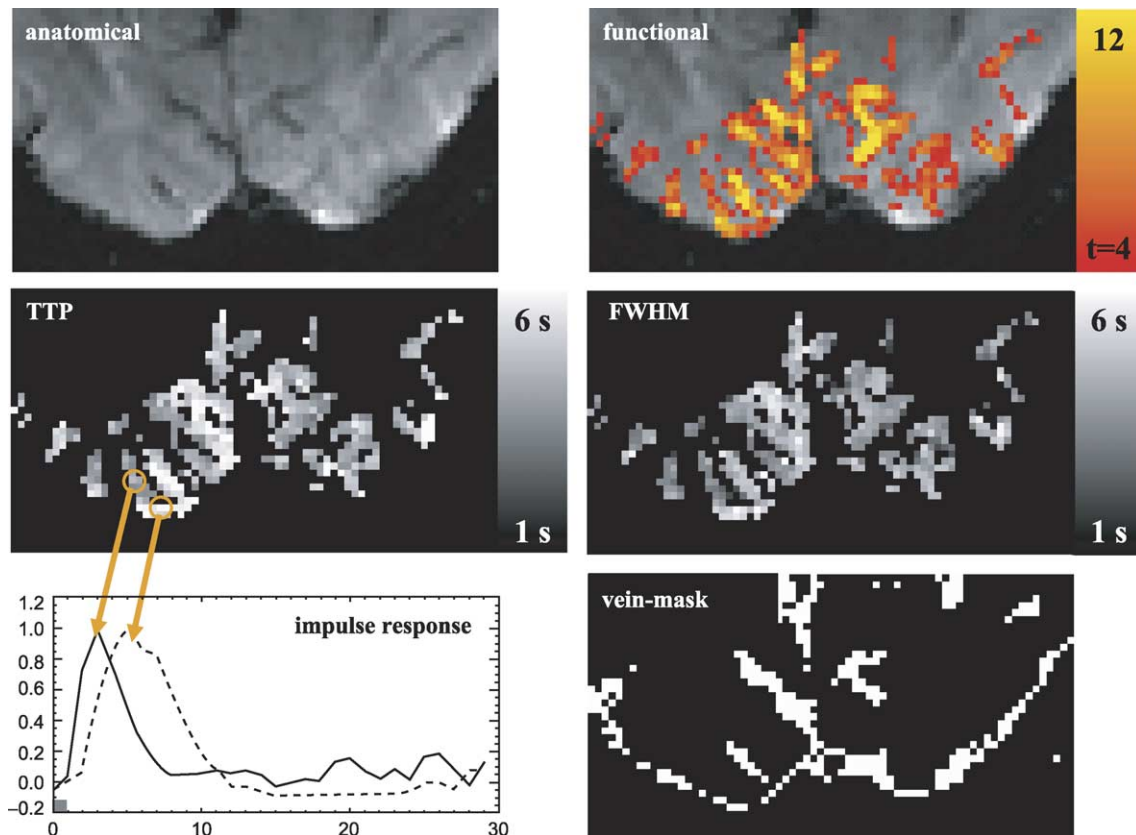

Fig. 4. Example of BOLD IR data from one of the human subjects. A single slice, parallel to the calcarine fissure, is shown. The top-left image shows an anatomical map of the visual cortex area (actual EPI data, resulting in low image contrast). The lower-left graph shows two HDR curves for two voxels with, respectively, a long and short TTP, demonstrating an increased FWHM for the curve with longer TTP. The lower-right image shows the vein-weighted mask. Note that the vein-weighted voxels are not randomly distributed but generally near the cortical surface.
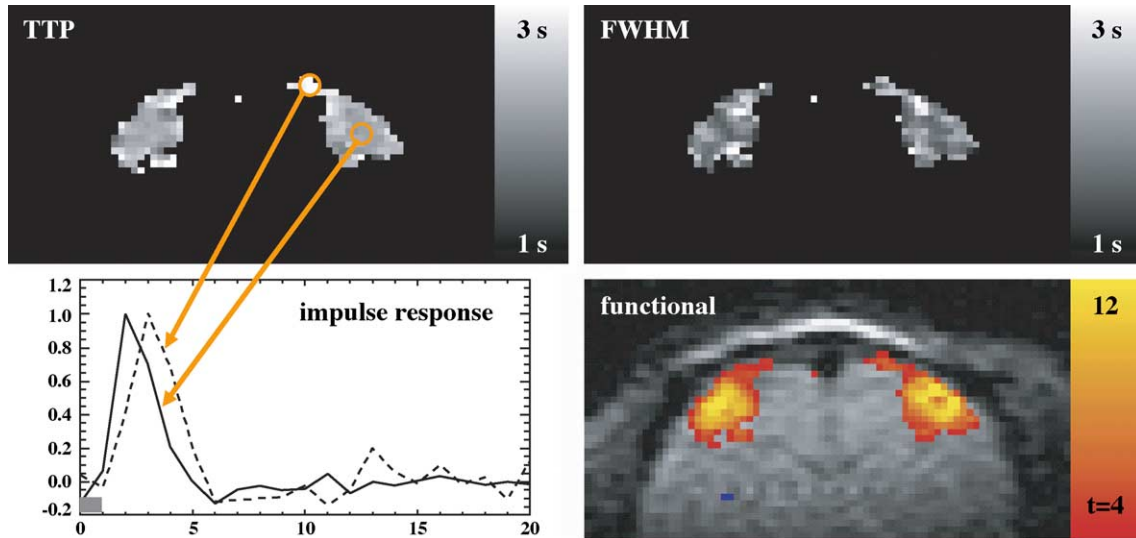
Fig. 5. Example of spatial distribution of TTP and FWHM values of the BOLD IR for rat somatosensory cortex (top left and right image, respectively). Although no significant correlation between TTP and FWHM was observed, pixels in the largest veins tended to have larger TTP and FWHM values. HDR curves for two pixels are shown, suggesting a somewhat longer TTP and FWHM in the middle cerebral vein compared to cortical grey matter.

Turner (2002) used Murray's law for computing the post-junction diameter of two merging vessels, which implies a linear dependence between flow velocity and vessel diameter, compared to the empirically determined relationship to the power 0.87 used here (see Appendix A). Use of a linear relationship in these simulations would result in a reduction of TTP and FWHM values (up to 37% for the 40-mm-long simulated flow path).

Also note that in these simulations, distances are calculated as the total traversed distance along the flow path, which in general is substantially longer than the Euclidian distance. Turner's (2002) paper does provide equations to compute the maximal distance from a cortical area of a given diameter (a circular activation patch is assumed) to its draining vein of certain diameter. This can be used to assess the range of Euclidian distances for the flow distances used in the simulation. For flow distances of 5, 10, 20, and 40 mm, the average Euclidian distances are, respectively, 3.2, 6.3, 12.7, and 25.3 mm. The minimal Euclidian distances from the capillary to the vessel locations in these simulations are, respectively, 1.3, 2.7, 5.3, and 10.6 mm. The maximal Euclidian distance is identical to the flow path length.

BOLD fMRI impulse response

In all human subjects ($n = 6$, 11 runs total), the sensitivity and stability of SENSE EPI acquisition technique were sufficient to detect the stimulus-induced activity in the early visual areas. Averaged over all runs, image SNR and percentage temporal SNR (average image intensity divided by temporal standard deviation) in visual cortex were 60.5 (± 7.8) and 38.4 (± 8.0), respectively. On average, 1221 pixels exceed the activation threshold (see Table 1). Within and across subjects, a substantial spread in TTP and FWHM values occurred. Across subjects, TTP and FWHM ranged from 3.99 to 5.72 and from 3.44 to 4.89, respectively.

An example of human TTP and FWHM maps, derived from impulse response estimates obtained with the m-sequence probe method, is shown in Fig. 4. Averaged over all subjects, TTP and FWHM were 4.51 ± 0.52 and 4.04 ± 0.42 s, respectively, see Table 1. There was a substantial variation in TTP and FWHM across the visual cortex, with intrasubject standard deviation (SD) averaging 0.79 for both TTP and FWHM. There was a significant correlation between TTP and FWHM, averaging 0.26 over all data sets (see Table 1). The average t score of this correlation was 9.41 (± 5.32), while the minimum t score was 3.80 ($P = 7.9 \times 10^{-5}$). This is also indicated by the slope of a fit of FWHM as a function of TTP (see Table 1) (assuming noise on both axes, see Numerical Recipes in C, p. 666, Press et al., 1992). This is in agreement with the linear TTP-FWHM relationship found in the simulation.

In rats, TTP and FWHM were substantially shorter and their spread (TTP SD) was much reduced (Fig. 5, Table 2). Average TTP and FWHM were 2.73 ± 0.60 and 2.28 ± 0.63 s, respectively.

Table 2
Temporal characteristics of BOLD fMRI IR in rats

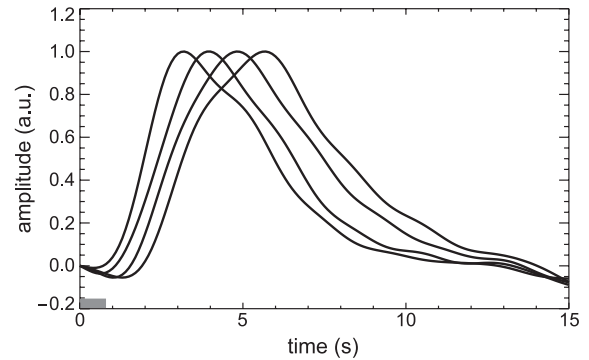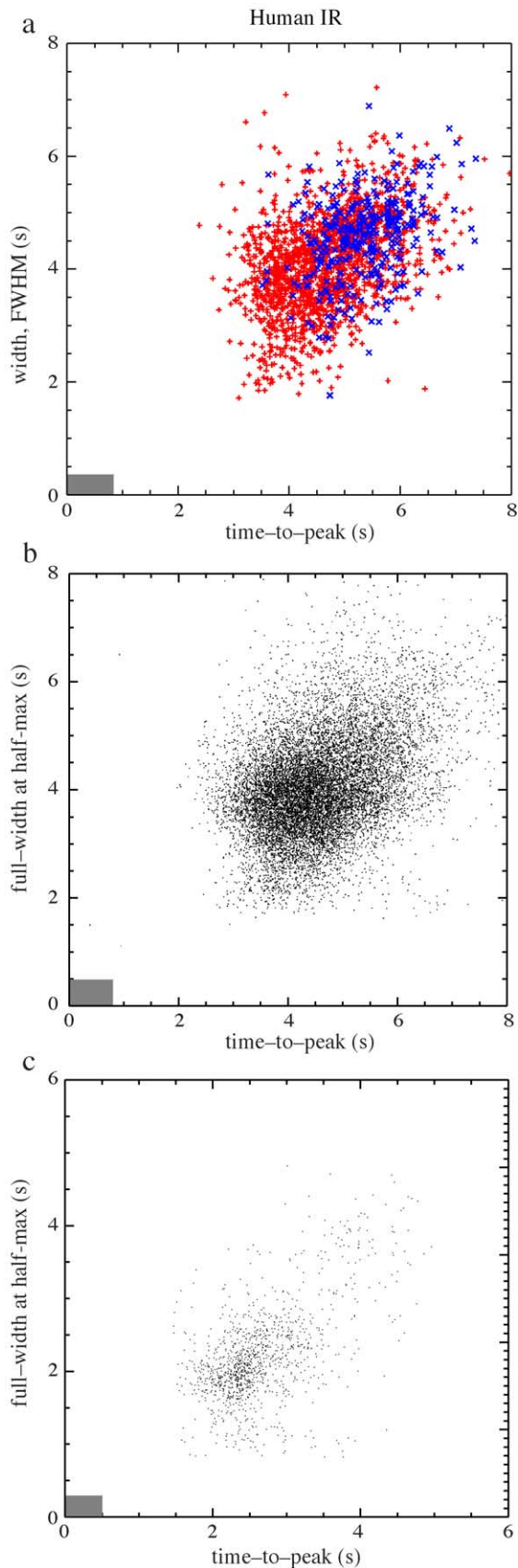| Rat	TTP (s)	TTP SD (s)	FWHM (s)	FWHM SD (s)	TTP vs. FWHM correlation	No. of pixels
1	2.41	0.13	1.93	0.11	0.25	143
2	3.36	0.15	2.83	0.13	0.59	97
3	3.94	0.38	3.59	0.35	0.11	75
4	2.33	0.17	2.03	0.15	0.15	83
5	2.68	0.50	2.31	0.43	0.39	290
6	2.36	0.37	1.91	0.30	0.09	204
7	2.31	0.35	1.81	0.28	−0.04	181
8	2.43	0.32	1.86	0.25	−0.31	130
Average (SD)	2.73 (0.60)	0.30	2.28 (0.63)	0.25	0.15 (0.27)	150 (76)

Human IR

Fig. 7. Temporal dispersion of the BOLD IR. Selectively averaged (see text) IR curves are shown, indicating the variation of IR shape as a function of TTP. These data demonstrate that voxels with longer TTP also have an increased FWHM.

There was no clear correlation between TTP and FWHM in rat (see Table 2, this correlation was significant, with $P < 0.01$, in only three out of eight data sets), although some pixels at the periphery of the somatosensory cortex and in the middle cerebral vein appeared to have an increased TTP. In separate experiments, gradient echo MR images of the imaging slice(s) clearly indicate the presence of a superficial vein running on the dorsal surface, from S1FL (the front limb area of the primary somatosensory cortex) toward the superior sagittal sinus (data not shown). The smaller area of activation found in rat will lead to a reduced contribution of vascular dispersion. This will lead to a reduced spread in TTP and FWHM in rat.

In most human subjects, a similarity was apparent between TTP and FWHM distribution patterns, with each pattern being dominated by intermediate spatial frequencies (i.e., clusters of several pixels diameter). Fig. 6 shows a scatter plot of FWHM vs. TTP for a single subject (a) and for all human (b) and rat (c) studies.

IR functions obtained from pixels in a vein-weighted ROI (blue pixels in Fig. 6a) had increased TTP and FWHM values as compared to pixels outside this ROI (red pixels in Fig. 6a). This difference is highly significant, a paired t test resulted in a t-value of 10.5 ($P = 9.7 \times 10^{-7}$) when comparing the average TTP inside the vein-weighted ROI with the TTP outside this ROI. The paired t test t value for the average FWHM was 5.7 ($P = 2.0 \times 10^{-4}$) for the same comparison. Averaged over all subjects, average TTP and FWHM values were 5.07 ± 0.64 and 4.33 ± 0.48 s for the vein-weighted ROI and 4.42 ± 0.52 and 3.98 ± 0.43 s for the voxels outside the vein-weighted ROI, respectively.

To investigate the dependence of impulse response shape (including FWHM) on TTP, human IR estimates were sorted on TTP value and selectively averaged for TTP bins in the range of 2–3, 3–4, 4–5, and 5–6 s, respectively. The covariance data, derived from correlation analysis, were averaged and then normalized. The resulting IR averages, shown in Fig. 7, confirm the correlation

Fig. 6. Correlation between IR TTP and FWHM values for BOLD fMRI. Points in scatter plots represent individual activated pixels. Grey bars in the lower-left corner of the plots indicate the duration of the stimuli. (a) Example of human data (single subject). Pixels in vein-weighted ROI (red points) are biased toward larger TTP and FWHM values as compared to all other pixels (blue points). (b) Composite plot of all human BOLD fMRI data. Every significantly activated pixel is indicated with (·). (c) Composite plot of all rat BOLD fMRI data.

between FWHM and TTP, with the later responses being broader. The same data were also averaged after noise weighting (*t* scores) and after scaling to the percentage of signal change (results not shown). Average *t* scores found for the four bins were similar; however, the percentage of average signal change (fractional signal change) increased with TTP. The observation that the average fractional signal change increase does not lead to an increase of the average *t* score suggests that the data in the 4th bin (the longest lag) consist of data with a higher temporal standard deviation. This supports our hypothesis for a higher venous contribution for higher TTP.

Discussion

General remarks

The data presented in this work demonstrate the feasibility to obtain a model-free measurement of the BOLD IR at high spatial resolution. To achieve this, sensitivity was improved by combining the *m*-sequence probe method with dedicated MRI technology, including the use of SENSE EPI and an optimized 16-channel brain array for the human experiments, and surface coil MRI at 11.7 T for the rat experiments. The fine spatial resolution facilitated investigation of the variation of the BOLD IR within a functional region. Furthermore, the availability of high-resolution EPI provided functional and anatomical (vein-sensitized) images with a precise spatial correspondence.

Contribution of macrovasculature to the IR

The BOLD fMRI measurements on human showed a substantial variation in IR timing within and across subjects. Regionally averaged TTP and FWHM values were in the range of those found in literature for short stimuli (Buckner, 1998; Pfeuffer et al., 2002). Note that the TTP and FWHM values were determined using 800-ms long stimuli. Longer stimuli (as often used in fMRI experiments) will lead to responses that further deviate (longer TTP and FWHM) from the true IR.

The variation of IR timing within human subjects within the primary visual cortex and the correlation between TTP and FWHM suggest a temporal dispersion in the macrovasculature. This despite the experimental conditions aimed at reducing contributions from within large veins, that is, long TR, vascular crusher gradients, and moderately high field (3.0 T). Simulations of the hemoglobin transit through the vasculature show that, depending on the flow velocity in the capillary bed, 1–2 s lengthening of TTP and FWHM can readily occur at a distance along the venous flow path of 20 mm. The increased TTP and FWHM values found in vein-weighted areas as determined intrinsically from the fMRI data are supportive of this "macrovascular dispersion hypothesis", although the amount of IR dispersion could not be fully explained from these analyses. This might be due to contamination of the vein-weighted areas with signals not originating from large veins. Note that the model assumes that every red blood cell contributes in the same way to the BOLD signal, independent of, for example, the orientation of the vessel and the location of the RBC in the vessel. Since a typical voxel will contain multiple vessels with different diameters and orientations, this model has limited validity in predicting the precise shape of an observed BOLD response.

In rats, significant temporal dispersion of the BOLD IR was found in only three out of eight rats. Several factors could have contributed to this finding, including a potentially reduced macrovascular contribution, a reduced spatial extent of the vasculature involved, differences in hemodynamics in anesthetized rats compared to awake humans, and differences in neurovascular control. Nevertheless, the reduced variation in IR timing in rats is unlikely to be entirely caused by a reduced macrovascular contribution. First of all, with the better than 4.2-μl resolution used in human experiments, a substantial number of voxels are entirely contained in the neuropil, and therefore relatively devoid of signal from large (pial) veins. However, almost all human TTP and FWHM values exceeded the average rat values of 2.73 and 2.28, respectively (see Fig. 6b). Furthermore, the rat data clearly contained contributions from large vessels, as can be seen in Fig. 5. A potential contributor to the observed differences in dispersion between humans and rats is a difference in flow velocity in the capillary/venous vasculature between rats and humans.

Ultimate temporal resolution of fMRI

In humans, and to a lesser extent in rats, the temporal resolution of BOLD fMRI is limited by the finite transit time for oxy-hemoglobin to travel through the macrovasculature. Provided MRI techniques can be designed to suppress macrovascular signals, the temporal resolution of the BOLD impulse response can likely be improved to 2–3 s FWHM in humans. This estimate is based on the spread in IR FWHM values in humans as well as the faster IR found in rats. At the same time, selection of the microvascular signal could lead to improved spatial resolution, as suggested in previous reports (Duyn et al., 1994; Kim et al., 2000; Lee et al., 1995). Some of the observed BOLD IR dispersion could also be incurred during the transit of blood through the capillary bed and toward the pial veins on the cortical surface. Functional MRI techniques that are not dependent on this transit effect, such as perfusion or blood-volume-weighted fMRI, potentially allow for further improved temporal resolution.

In conclusion, the data presented indicate that BOLD fMRI temporal resolution is generally limited by hemoglobin transit effects in the venous vasculature. This has important implications for the interpretation of BOLD fMRI, in particular with regards to inferences about timing of neuronal processes. In the absence of hemoglobin transit effects, the ultimate BOLD fMRI resolution likely approaches the time scale of the neurovascular control mechanism, which is partly dependent on a diffusion process involving chemical messengers such as nitrous oxide (Dreier et al., 1995), and possibly a successive spread of dilation to upstream arteries (Iadecola et al., 1997; Segal and Duling, 1986). The onset of the cortical blood volume increase has been found to be in the range of 400–800 ms (Frostig et al., 1990; Vanzetta and Grinvald, 2001). However, the temporal characteristics of the IR of neurovascular control need to be firmly established to determine the ultimate fMRI temporal resolution.

Appendix A. Equations used for simulation of post-capillary blood flow

The vessel diameter as a function of distance from the capillary bed was derived from Eq. 9 in Turner (2002):

$$d = \frac{\left(\frac{1000y}{35}\right)^{2/3}}{1000} \approx 0.0093y^{2/3}, \tag{A1}$$

where d is the diameter of the vessel in m and y the distance from the capillary bed in m. Note that factor 1000, which appears twice in this equation, is the result of expressing both d and y in m in stead of mm. The relationship between vessel diameter and flow was derived from the empirical relationship found by Hudetz (1992):

$$F_c = KD^{2.87} \tag{A2}$$

where K is a constant, D is the vessel diameter in μm, and F_c the red blood cell flow in ml s^{-1}. This equation can be adapted to compute the average red blood cell flow velocity, assuming that the vessel is round (and therefore has a vessel cross-sectional area of π $(0.5d)^2$):

$$v_{avg} = \frac{kd^{2.87}}{\pi(0.5d)^2} = \frac{4}{\pi}kd^{0.87}, \tag{A3}$$

where v_{avg} is the average flow velocity (in m s^{-1}) for the given capillary diameter d (in m), and k is a constant that can be computed from capillary diameter and flow velocity as

$$k = \frac{\pi}{4}v_{avg,cap}\left(d_{cap}\right)^{-0.87}, \tag{A4}$$

where d_{cap} is the diameter of the capillary and $v_{avg,cap}$ the average flow velocity in the capillary. Based on the notion that the overall flow before and after a bifurcation must remain constant, Eq. (A2) can be used to derive the diameter of the vessel that is formed as the result of two vessels of identical size combining:

$$\frac{d_{post\text{-}junction}}{d_{pre\text{-}junction}} = 2^{(1/2.87)} \tag{A5}$$

where $d_{post\text{-}junction}$ is the diameter of the vessel that is formed by merging two vessels with diameter $d_{pre\text{-}junction}$. Based on Eq. (A1), the separation of mixing points subsequently scales as:

$$\frac{y_{post\text{-}junction}}{y_{pre\text{-}junction}} = 2^{(1/2.87)(3/2)} = 2^{(3/5.74)} \tag{A6}$$

where $y_{pre\text{-}junction}$ and $y_{post\text{-}junction}$ are the (junction-to-junction) section lengths surrounding a given bifurcation.

References

Aguirre, G.K., Zarahn, E., D'Esposito, M., 1998. The variability of human. BOLD hemodynamic responses. NeuroImage 8, 360–369.

Belliveau, J.W., Kennedy Jr., D.N., McKinstry, R.C., Buchbinder, B.R., Weisskoff, R.M., Cohen, M.S., Vevea, J.M., Brady, T.J., Rosen, B.R., 1991. Functional mapping of the human visual cortex by magnetic resonance imaging. Science 254, 716–719.

Berwick, J., Martin, C., Martindale, J., Jones, M., Johnston, D., Zheng, Y., Redgrave, P., Mayhew, J., 2002. Hemodynamic response in the unanesthetized rat: intrinsic optical imaging and spectroscopy of the barrel cortex. J. Cereb. Blood Flow Metab. 22, 670–679.

Bodurka, J., Ledden, P.J., van Gelderen, P., Chu, R., de Zwart, J.A., Morris, D., Duyn, J.H., 2004. Scalable multichannel MRI data acquisition system. Magn. Reson. Med. 51, 165–171.

Boynton, G.M., Engel, S.A., Glover, G.H., Heeger, D.J., 1996. Linear systems analysis of functional magnetic resonance imaging in human V1. J. Neurosci. 16, 4207–4221.

Bruder, H., Fischer, H., Reinfelder, H.E., Schmitt, F., 1992. Image reconstruction for echo planar imaging with nonequidistant k-space sampling. Magn. Reson. Med. 23, 311–323.

Buckner, R.L., 1998. Event-related fMRI and the hemodynamic response. Hum. Brain Mapp. 6, 373–377.

Buracas, G.T., Boynton, G.M., 2002. Efficient design of event-related fMRI experiments using M-sequences. NeuroImage 16, 801–813.

Chaigneau, E., Oheim, M., Audinat, E., Charpak, S., 2003. Two-photon imaging of capillary blood flow in olfactory bulb glomeruli. Proc. Natl. Acad. Sci. U. S. A. 100, 13081–13086.

Cheng, K., Waggoner, R.A., Tanaka, K., 2001. Human ocular dominance columns as revealed by high-field functional magnetic resonance imaging. Neuron 32, 359–374.

Cohen, E.R., Ugurbil, K., Kim, S.G., 2002. Effect of basal conditions on the magnitude and dynamics of the blood oxygenation level-dependent fMRI response. J. Cereb. Blood Flow Metab. 22, 1042–1053.

de Zwart, J.A., Van Gelderen, P., Kellman, P., Duyn, J.H., 2002. Application of sensitivity-encoded echo-planar imaging for blood oxygen level-dependent functional brain imaging dagger. Magn. Reson. Med. 48, 1011–1020.

de Zwart, J.A., Ledden, P.J., van Gelderen, P., Bodurka, J., Chu, R., Duyn, J.H., 2004. Signal-to-noise ratio and parallel imaging performance of a 16-channel receive-only brain coil array at 3.0 Tesla. Magn. Reson. Med. 51, 22–26.

Dreier, J.P., Korner, K., Gorner, A., Lindauer, U., Weih, M., Villringer, A., Dirnagl, U., 1995. Nitric oxide modulates the CBF response to increased extracellular potassium. J. Cereb. Blood Flow Metab. 15, 914–919.

Dunn, A.K., Devor, A., Bolay, H., Andermann, M.L., Moskowitz, M.A., Dale, A.M., Boas, D.A., 2003. Simultaneous imaging of total cerebral hemoglobin concentration, oxygenation, and blood flow during functional activation. Opt. Lett. 28, 28–30.

Duong, T.Q., Kim, D.S., Ugurbil, K., Kim, S.G., 2001. Localized cerebral blood flow response at submillimeter columnar resolution. Proc. Natl. Acad. Sci. U. S. A. 98, 10904–10909.

Duong, T.Q., Yacoub, E., Adriany, G., Hu, X., Ugurbil, K., Kim, S.G., 2003. Microvascular BOLD contribution at 4 and 7 T in the human brain: gradient-echo and spin-echo fMRI with suppression of blood effects. Magn. Reson. Med. 49, 1019–1027.

Duvernoy, H.M., Delon, S., Vannson, J.L., 1981. Cortical blood vessels of the human brain. Brain Res. Bull. 7, 519–579.

Duyn, J.H., Moonen, C.T., van Yperen, G.H., de Boer, R.W., Luyten, P.R., 1994. Inflow versus deoxyhemoglobin effects in BOLD functional MRI using gradient echoes at 1.5 T. NMR Biomed. 7, 83–88.

Engel, S.A., Glover, G.H., Wandell, B.A., 1997. Retinotopic organization in human visual cortex and the spatial precision of functional MRI. Cereb. Cortex 7, 181–192.

Friston, K.J., Jezzard, P., Turner, R., 1994. The analysis of functional MRI time-series. Hum. Brain Mapp. 1, 153–171.

Frostig, R.D., Lieke, E.E., Ts'o, D.Y., Grinvald, A., 1990. Cortical functional architecture and local coupling between neuronal activity and the microcirculation revealed by in vivo high-resolution optical imaging of intrinsic signals. Proc. Natl. Acad. Sci. U. S. A. 87, 6082–6086.

Hoge, R.D., Atkinson, J., Gill, B., Crelier, G.R., Marrett, S., Pike, G.B., 1999. Investigation of BOLD signal dependence on cerebral blood flow and oxygen consumption: the deoxyhemoglobin dilution model. Magn. Reson. Med. 42, 849–863.

Hudetz, A.G., 1992. Computer simulation of erythrocyte transit in the cerebrocortical capillary network. Adv. Exp. Med. Biol. 317, 659–670.

Hudetz, A.G., Feher, G., Weigle, C.G., Knuese, D.E., Kampine, J.P., 1995. Video microscopy of cerebrocortical capillary flow: response to

hypotension and intracranial hypertension. Am. J. Physiol. 268, H2202–2210.

Iadecola, C., Yang, G., Ebner, T.J., Chen, G., 1997. Local and propagated vascular responses evoked by focal synaptic activity in cerebellar cortex. J. Neurophysiol. 78, 651–659.

Kellman, P., Gelderen, P., de Zwart, J.A., Duyn, J.H., 2003. Method for functional MRI mapping of nonlinear response. NeuroImage 19, 190–199.

Kim, S.G., Richter, W., Ugurbil, K., 1997. Limitations of temporal resolution in functional MRI. Magn. Reson. Med. 37, 631–636.

Kim, D.S., Duong, T.Q., Kim, S.G., 2000. High-resolution mapping of iso-orientation columns by fMRI. Nat. Neurosci. 3, 164–169.

Kleinfeld, D., Mitra, P.P., Helmchen, F., Denk, W., 1998. Fluctuations and stimulus-induced changes in blood flow observed in individual capillaries in layers 2 through 4 of rat neocortex. Proc. Natl. Acad. Sci. U. S. A. 95, 15741–15746.

Krimer, L.S., Muly III, E.C., Williams, G.V., Goldman-Rakic, P.S., 1998. Dopaminergic regulation of cerebral cortical microcirculation. Nat. Neurosci. 1, 286–289.

Krolo, I., Hudetz, A.G., 2000. Hypoxemia alters erythrocyte perfusion pattern in the cerebral capillary network. Microvasc. Res. 59, 72–79.

Kruggel, F., von Cramon, D.Y., 1999. Temporal properties of the hemodynamic response in functional MRI. Hum. Brain Mapp. 8, 259–271.

Lee, A.T., Glover, G.H., Meyer, C.H., 1995. Discrimination of large venous vessels in time-course spiral blood-oxygen-level-dependent magnetic-resonance functional neuroimaging. Magn. Reson. Med. 33, 745–754.

Logothetis, N.K., Pauls, J., Augath, M., Trinath, T., Oeltermann, A., 2001. Neurophysiological investigation of the basis of the fMRI signal. Nature 412, 150–157.

Ma, Y.P., Koo, A., Kwan, H.C., Cheng, K.K., 1974. On-line measurement of the dynamic velocity of erythrocytes in the cerebral microvessels in the rat. Microvasc. Res. 8, 1–13.

Menon, R.S., Luknowsky, D.C., Gati, J.S., 1998. Mental chronometry using latency-resolved functional MRI. Proc. Natl. Acad. Sci. U. S. A. 95, 10902–10907.

Miezin, F.M., Maccotta, L., Ollinger, J.M., Petersen, S.E., Buckner, R.L., 2000. Characterizing the hemodynamic response: effects of presentation rate, sampling procedure, and the possibility of ordering brain activity based on relative timing. NeuroImage 11, 735–759.

Nakai, K., Imai, H., Kamei, I., Itakura, T., Komari, N., Kimura, H., Nagai, T., Maeda, T., 1981. Microangioarchitecture of rat parietal cortex with special reference to vascular "sphincters". Scanning electron microscopic and dark field microscopic study. Stroke 12, 653–659.

Nehls, V., Drenckhahn, D., 1993. The versatility of microvascular pericytes: from mesenchyme to smooth muscle? Histochemistry 99, 1–12.

Ogawa, S., Lee, T.M., Kay, A.R., Tank, D.W., 1990. Brain magnetic resonance imaging with contrast dependent on blood oxygenation. Proc. Natl. Acad. Sci. U. S. A. 87, 9868–9872.

Ogawa, S., Lee, T.M., Stepnoski, R., Chen, W., Zhu, X.H., Ugurbil, K., 2000. An approach to probe some neural systems interaction by functional MRI at neural time scale down to milliseconds. Proc. Natl. Acad. Sci. U. S. A. 97, 11026–11031.

Pfeuffer, J., van de Moortele, P.F., Yacoub, E., Shmuel, A., Adriany, G.,

Andersen, P., Merkle, H., Garwood, M., Ugurbil, K., Hu, X., 2002. Zoomed functional imaging in the human brain at 7 Tesla with simultaneous high spatial and high temporal resolution. NeuroImage 17, 272–286.

Press, W.H., Teukolsky, S.A., Vetterling, W.T., Flannery, B.P., 1992. Numerical Recipes in C—The Art of Scientific Computing.

Pruessmann, K.P., Weiger, M., Scheidegger, M.B., Boesiger, P., 1999. SENSE: sensitivity encoding for fast MRI. Magn. Reson. Med. 42, 952–962.

Reinhard Jr., J.F., Liebmann, J.E., Schlosberg, A.J., Moskowitz, M.A., 1979. Serotonin neurons project to small blood vessels in the brain. Science 206, 85–87.

Rosenblum, W.I., 1971. Erythrocyte velocity and fluorescein transit time in the cerebral microcirculation of macroglobulinemic mice: differential effect of a hyperviscosity syndrome on the passage of erythrocytes and plasma. Microvasc. Res. 3, 288–296.

Rudin, M., Beckmann, N., Sauter, A., 1997. Analysis of tracer transit in rat brain after carotid artery and femoral vein administrations using linear system theory. Magn. Reson Imaging 15, 551–558.

Segal, S.S., Duling, B.R., 1986. Flow control among microvessels coordinated by intercellular conduction. Science 234, 868–870.

Shoham, D., Grinvald, A., 2001. The cortical representation of the hand in macaque and human area S-I: high resolution optical imaging. J. Neurosci. 21, 6820–6835.

Silva, A.C., Koretsky, A.P., 2002. Laminar specificity of functional MRI onset times during somatosensory stimulation in rat. Proc. Natl. Acad. Sci. U. S. A. 99, 15182–15187.

Silva, A.C., Lee, S.P., Yang, G., Iadecola, C., Kim, S.G., 1999. Simultaneous blood oxygenation level-dependent and cerebral blood flow functional magnetic resonance imaging during forepaw stimulation in the rat. J. Cereb. Blood Flow Metab. 19, 871–879.

Sutter, E.E., 2001. Imaging visual function with the multifocal m-sequence technique. Vision Res. 41, 1241–1255.

Thierry, G., Boulanouar, K., Kherif, F., Ranjeva, J.P., Demonet, J.F., 1999. Temporal sorting of neural components underlying phonological processing. NeuroReport 10, 2599–2603.

Turner, R., 2002. How much cortex can a vein drain? Downstream dilution of activation-related cerebral blood oxygenation changes. NeuroImage 16, 1062–1067.

Vanzetta, I., Grinvald, A., 2001. Evidence and lack of evidence for the initial dip in the anesthetized rat: implications for human functional brain imaging. NeuroImage 13, 959–967.

Vaucher, E., Hamel, E., 1995. Cholinergic basal forebrain neurons project to cortical microvessels in the rat: electron microscopic study with anterogradely transported Phaseolus vulgaris leucoagglutinin and choline acetyltransferase immunocytochemistry. J. Neurosci. 15, 7427–7441.

Villringer, A., Them, A., Lindauer, U., Einhaupl, K., Dirnagl, U., 1994. Capillary perfusion of the rat brain cortex. An in vivo confocal microscopy study. Circ. Res. 75, 55–62.

Zonta, M., Angulo, M.C., Gobbo, S., Rosengarten, B., Hossmann, K.A., Pozzan, T., Carmignoto, G., 2003. Neuron-to-astrocyte signaling is central to the dynamic control of brain microcirculation. Nat. Neurosci. 6, 43–50.